

# Two-photon Rydberg EIT resonances in non-collinear beam configurations

KEVIN SU<sup>1</sup>, ROB BEHARY<sup>1</sup>, SETH A. AUBIN<sup>1</sup>, EUGENIY E. MIKHAILOV<sup>1</sup>, AND IRINA NOVIKOVA<sup>1</sup>

<sup>1</sup>Dept. of Physics, William & Mary, Williamsburg, VA 23187 USA

Compiled December 2, 2024

We study the modifications of Rydberg EIT resonances in non-collinear geometry, in which the two required optical fields cross at a small non-zero angle. We observe a strong broadening and amplitude reduction even for small angles, when compared to exact counter-propagating and co-propagating collinear geometries. We confirm that such EIT peak deterioration results from the additional Doppler broadening due the transverse velocity distribution atoms. The numerical simulation closely matches the experimental measurements. While a non-collinear geometry provides improved spatial resolution for Rydberg EIT electrometry, we conclude that the crossing angle must be small to maintain field sensitivity.

<http://dx.doi.org/10.1364/ao.XX.XXXXXX>

Rydberg states – electron orbitals with high principle quantum number  $n \geq 20$  – have many attractive properties, most notably a long lifetime and large electric dipole moment and polarizability [1]. The resulting sensitivity to external electromagnetic fields makes them excellent candidates for atom-based electrometry applications. The ability to measure spectroscopic shifts, caused by the interaction with an electric field, via optical means and in thermal atomic vapor further improves their attractiveness for practical applications. Indeed, many research groups have already demonstrated Rydberg state-based tools such as an SI-traceable electric field standard [2], in-situ detectors for dc and rf-electric fields [3–5], THz imaging [6–8], etc.

A majority of these applications rely on a non-linear two-photon process known as electromagnetically induced transparency (EIT) [9–11], in which atoms are prepared in a superposition of the ground and Rydberg states that leads to reduced absorption for the probe optical field. The spectral width of the Rydberg EIT resonance is relatively narrow, so keeping track of its spectral shift or splitting allows for monitoring the electromagnetic environment in real time. In a thermal vapor with Doppler broadening, the Rydberg EIT resonance is narrowest when the two laser beams are collinear: In this geometry, the spectral shifts are integrated over the length of the laser beams, which enhances the signal but limits its spatial resolution.

In this paper, we investigate experimentally two non-collinear Rydberg EIT geometries, nearly counter-propagating and nearly co-propagating, to determine the extent of the trade-off between spatial and spectral resolution. Our motivation for this work is to use Rydberg EIT to map out spatial variations of electric and magnetic fields, e.g., due to an electron beam [12] or in a low-density plasma [13]. The main result of this paper is

that the loss in spectral resolution and signal strength happens relatively quickly as the angle between the lasers is increased, and thus a small-angle non-collinear geometry is preferred.

In our experiments we implemented Rydberg EIT in a <sup>85</sup>Rb vapor cell, using two laser fields in a ladder configuration, shown in Fig.1(a). The infrared probe laser ( $\lambda_P \simeq 780$  nm, beam diameter  $d = 0.6$  mm) is tuned to the  $5S_{1/2} F = 3 \rightarrow 5P_{3/2} F'$  optical transition, and its transmission through a Rb cell is monitored to detect the EIT resonances. For this experiments we used a cylindrical glass cell (diameter  $D = 2$  cm, length  $L_{cell} = 2.5$  cm), heated to 37°C. The coupling laser ( $\lambda_C \simeq 480$  nm, beam diameter  $d = 0.6$  mm) connects the state  $5P_{3/2}$  with the Rydberg states  $45D_{3/2}$  or  $45D_{5/2}$ .

To satisfy the two-photon resonance conditions, the sum of these two laser frequencies  $\omega_P$  and  $\omega_C$  must match the energy splitting between the ground and the Rydberg state  $\omega_{gr}$ . The absorption reduction, associated with EIT, is observable only in a narrow spectral range of two-photon detuning values  $\delta_0 = \omega_P + \omega_C - \omega_{gr} \leq \gamma_{EIT}$ . For stationary atoms the EIT linewidth  $\gamma_{EIT}$  is limited by the relaxation rate of the Rydberg state and the power broadening, and can be quite narrow (a few hundred kHz). However, in a thermal ensemble one must account for the Doppler shift, yieldings to the velocity dependence of the two-photon detuning:

$$\delta(\vec{v}) = (\omega_P + \omega_C - \omega_{gr}) - (\vec{k}_P + \vec{k}_C) \cdot \vec{v}, \quad (1)$$

where the detunings  $\Delta_P = \omega_P - \omega_{ge}$  and  $\Delta_C = \omega_C - \omega_{er}$  are determined as the frequency difference of the probe and coupling optical field and the corresponding optical transitions,  $\vec{k}_P$  and  $\vec{k}_C$  are the wave vectors of the correspondingly probe and coupling laser fields, and  $\vec{v}$  is the velocity of a Rb atom. Because

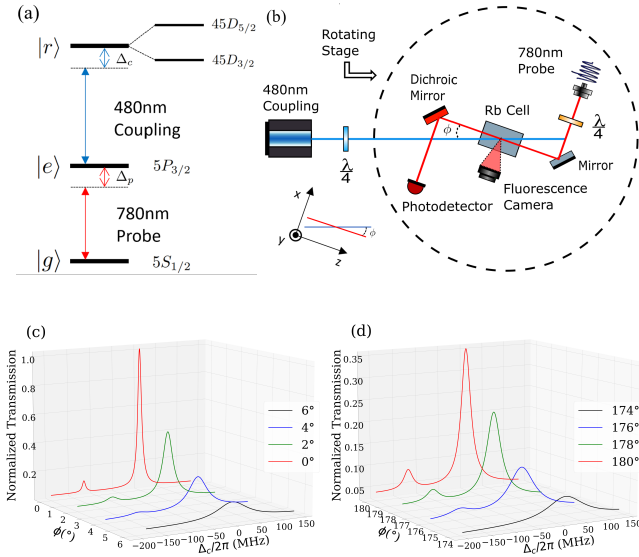


**Fig. 1.** (a) Energy level diagram of  $^{85}\text{Rb}$ . Probe beam couples to the  $D_2$  line of  $^{85}\text{Rb}$ , and the coupling beam excites atoms to the  $45D$  Rydberg state. (b) Experimental setup diagram. (c) Traces of EIT resonances recorded with nearly counter-propagating probe and coupling fields, crossing at a small angle  $\phi \approx 0$ . Probe laser frequency is locked to the bottom of the  $^{85}\text{Rb}$   $F = 3 \rightarrow F'$  optical transition, and the coupling frequency is scanned across transitions to the  $45D_{5/2}$  state (taller peak) and  $45D_{3/2}$  (smaller peak). For all transmission spectra the zero coupling laser detuning is set to zero at the top of the  $45D_{5/2}$  EIT resonance. (d) Same as (c) but for nearly co-propagating laser beams ( $\phi \approx 180^\circ$ ). In both cases (c) and (d), the transmission is normalized to the highest transmission observed at zero detuning and  $\phi = 0$ .

of the significant difference in the wavelength values for the two lasers, it is impossible to completely suppress the Doppler effect by optimizing the relative orientation of the two laser beams (although it is possible for three-photon EIT configurations [14–16]). Obviously, the maximum suppression happens for counter-propagating laser beams. This is a common arrangement in most experiments, involving Rydberg EIT in hot atoms, resulting in minimum achievable EIT linewidth to be around a few MHz [17, 18]. However, such geometry requires perfect spatial overlap of the laser beams, so any response to the measured electric field is integrated along the beam path.

On the other hand, crossing the laser beams at a specific location can be used to measure a local value of the spatially varying electric field. The motivation for this study is to experimentally study the modification of EIT peak as we deviate from the counter-propagating beam arrangement and send beams crossing at some angle  $\phi$ . In this case the velocity dependence of the two-photon detuning becomes even more complicated, as it depends on not only longitudinal  $v_{\parallel}$  but also on the transverse component  $v_{\perp}$  of the atomic velocity relative to the probe beam propagation direction:

$$\delta(\vec{v}) = \delta_0 - (k_P - k_C \cos\phi) v_{\parallel} + k_C \sin\phi v_{\perp}, \quad (2)$$

where  $\delta_0 = \Delta_P + \Delta_C$  is the two-photon detuning. In the following discussion we use the direction of the probe vector as the reference, and define the angle  $\phi$  as the angle between the

two beams. Note that we set  $\phi = 0^\circ$  to correspond to the more standard counter-propagating beam orientation, while  $\phi = 180^\circ$  refers to co-propagating probe and coupling beams. When changing the angle between the beams, we observe significant broadening of EIT resonance, as well as rapid reduction of its amplitude for even a few degree angle.

The schematic of the experimental arrangement is shown in Fig.1(b). We use external cavity diode lasers for both optical fields. The fiber-coupled output of the probe laser (power  $P_P = 70 \mu\text{W}$ ), the Rb vapor cell, and the amplified photodetector used to measure the output probe field power are mounted on the rotational platform, so that their relative positions are unchanged during the measurements. Co- or counter-propagating coupling laser (power  $P_C = 35 \text{ mW}$ ) is aligned through the cell such as the rotating of the platform keeps the laser beams intercept in the middle of the Rb cell. Such arrangement allows us to precisely control the angle between the two laser beams, and to reduce any non-EIT related changes in the probe laser transmission. In both geometries we use circularly polarized laser beams. The total variation of the transmitted coupling laser power for  $\phi = 0 - 8^\circ$  is less than 3%, and has negligible effect on the observed resonance modifications.

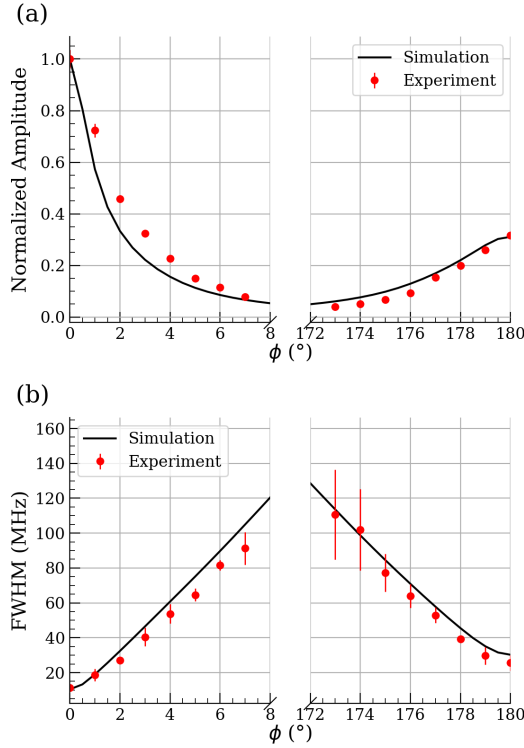
Strong angular dependence of EIT resonances is illustrated in Fig.1(c,d). When plotting transmission spectra, we subtract the background and use the hyperfine splitting of the  $45D_{5/2}$  and  $45D_{3/2}$  hyperfine splitting as a frequency reference, and for each trace set the zero detuning at the top of the  $45D_{5/2}$  EIT resonance. As expected, the counter-propagating laser beams produce highest and narrowest transmission peak. The co-propagating geometry leads to approximately 30% reduction in the resonance amplitude, and approximately doubles the resonance linewidth. However, in both geometries even a small deviation from the collinear geometry has strong effect, broadening and weakening the EIT resonance. For example, a smaller EIT peak due to coupling to the  $45D_{3/2}$  state almost completely disappears for angles above  $5^\circ$ .

Fig.2 shows a more quantitative way to analyze the variation of the EIT resonance amplitude and width as functions of the small beam deviation for the co- or counter-propagating geometries. In this results we normalized all the resonance amplitude to its value in a counter-propagating geometry, for easier comparison. It is also important to note that there may be some unintentional systematic variation between the two geometries, even though we tried to maintain all the experimental parameters identical, as the change of the geometry required setup realignment. However, in both cases the amplitude values drop below 20% of the collinear configurations with the crossing angle as small as  $5^\circ$ . Simultaneously, the width of the resonance triples. Such behavior can be qualitatively explained by analyzing the contributions of different velocity groups of atoms into the overall optical response.

To gain some intuition, we can consider a simple ladder interaction scheme, shown in Fig.1(a), the probe linear susceptibility  $\chi_P$  of an ensemble of  $N$  atoms per unit volume (see, e.g., [10, 19]):

$$\chi_P = \alpha_0 \frac{i\gamma}{\gamma - i\Delta_P} \left[ 1 - \frac{\Omega_C^2}{4(\gamma_r - i\Delta_P - i\Delta_C)(\gamma - i\Delta_P) + \Omega_C^2} \right], \quad (3)$$

where  $\alpha_0 = \frac{N\mu_P^2}{\hbar\epsilon_0}$  is the unsaturated resonant absorption for a two-level system (here  $\mu_P$  is the dipole moment of the  $g - e$  optical transition),  $\gamma$  and  $\gamma_r$  are the decay rates of correspondingly excited and Rydberg states,  $\Omega_C$  is the Rabi frequency of



**Fig. 2.** Comparison of amplitude (a) and full width at half maximum (b) of the main EIT resonance (coupling to the  $45D_{5/2}$  Rydberg state) between experiment and Rydiqule simulation. The simulation parameters are: Rabi frequencies  $\Omega_P = 7.9$  MHz and  $\Omega_C = 1.2$  MHz, intermediate state lifetimes (from ARC)  $\gamma = 6$  MHz and Rydberg state lifetime  $\gamma_r = 1$  kHz, and atomic density  $N = 8.5 \times 10^{16} \text{ m}^{-3}$ .

the coupling optical field, and we assume that the probe field Rabi frequency is small. From this equation it is easy to see that the probe field absorption signal consists of a one-photon absorption with the width set by the lifetime of the intermediate state  $\gamma$ , superposed with an additional narrow reduction of absorption, proportional to the control field, manifesting electromagnetically induced transparency, with the width determined by the Rydberg state lifetime and the control field intensity  $\gamma_{EIT} \sim \gamma_r + \Omega_C^2/\gamma$ . As discussed above, for moving atoms we need to account for the Doppler effect:  $\Delta_P \rightarrow \Delta_P - \vec{k}_P \vec{v}$ ,  $\Delta_C \rightarrow \Delta_C - \vec{k}_C \vec{v}$ . In the collinear geometry, only the velocity component along the laser beam propagation direction affects the two-photon detuning  $\delta$ :

$$\delta_{\text{coll}} = \delta_0 - (k_P \pm k_C)v_{\parallel}, \quad (4)$$

where  $\pm$  indicates counter- or co-propagating geometry. Consequently, each atomic velocity class contributes differently to the overall absorption profile (see [10] for the detailed discussion). Assuming for simplicity a resonant coupling field  $\Delta_C = 0$ , it is easy to see that only a relatively small fraction of atoms with  $|v_{\parallel}| \leq \gamma/k_P$  absorbs the probe optical field. Among those, even smaller group of relatively slow atoms  $|v_{\parallel}| \leq \gamma_{EIT}/(k_P \pm k_C)$  contribute to the resulting EIT resonance around  $\Delta_P = 0$ . Differences in the exact EIT peak positions for each velocity group results in a broader and lower contrast peak than that for cold atoms. However, in the collinear geometry atomic transverse velocity does not affect their optical response, so all the

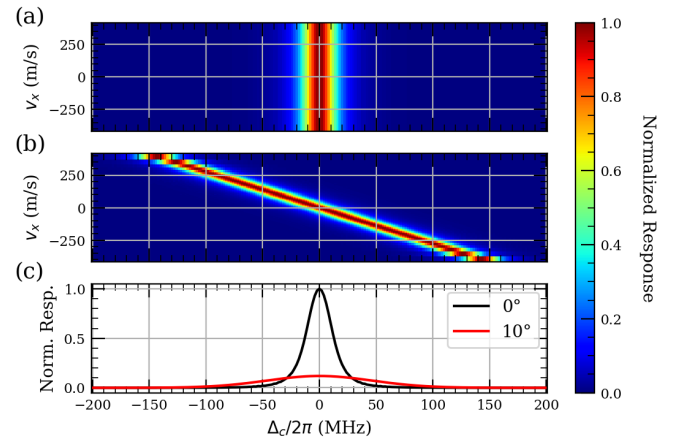


**Fig. 3.** Illustration of the transverse velocity distribution on EIT resonances in various geometries. (a) and (b) show the relative optical transmission (normalized to its maximum) for different transverse velocity groups as a function of the coupling laser detuning. In a collinear geometry  $\phi = 0$  (a) the frequency of the EIT resonances does not depend on  $v_{\perp}$ , so all transverse velocity groups contribute identically. For non-collinear geometry  $\phi = 10^\circ$  (b) the EIT peak for each velocity group is shifted by the amount proportional to its transverse velocity  $\delta_{EIT}(v_{\perp}) = -k_C v_{\perp} \sin \phi$ . (c) Resulting EIT peak averaged over the Maxwell distribution of  $v_{\perp}$  for  $\phi = 0$  and  $\phi = 10^\circ$ .

atoms with same  $v_{\parallel}$  but different  $v_{\perp}$  contribute the same way, as illustrated in Fig.3(a).

The situation is different if there is an angle  $\phi$  between the laser beams. Only the atoms with the zero two-photon detuning Eq.2 contribute to the EIT peak. While the small angle between the laser beams  $\phi$  hardly affects the dependence on the longitudinal atomic velocity (since  $\cos \phi \approx 1$  for  $\phi \ll 1$ ), the non-zero transverse velocity effectively changes the resonance position. Specifically, when averaged over the longitudinal velocity distribution, for each transverse velocity group the EIT peak occurs at the two-photon detuning  $\delta_{EIT}(v_{\perp}) = -k_C v_{\perp} \sin \phi$ , as illustrated in Fig.3(b). Averaging over the Doppler transverse velocity distribution results in a substantial additional broadening of the EIT peak and corresponding reduction in the EIT resonance amplitude, as shown in Fig.3(c). One can roughly estimate the EIT peak linewidth increase at a small angle  $\phi$  between the probe and coupling beams as  $\gamma_{EIT}(\phi) = \sqrt{\gamma_{EIT}^2(0) + (k_C v_D \sin \phi)^2}$ , where  $\gamma_{EIT}^2(0)$  is the width of EIT resonance for a collinear geometry. Same is true for the nearly co-propagating beams by replacing  $\gamma_{EIT}^2(0)$  with  $\gamma_{EIT}^2(180^\circ)$ .

While this simplified and idealized picture provides some intuition about the EIT resonance properties in non-collinear geometry, more accurate model is required to achieve quantitative agreement with the experimental data. For this model we still rely on the simplified ladder interaction scheme shown in Fig. 1(a), but use the parameters close to the experimental value, and include interaction with both  $45D_{5/2}$  and  $45D_{3/2}$  Rydberg hyperfine levels. In this case, the interaction Hamiltonian can be

written as:

$$H = \frac{\hbar}{2} \begin{pmatrix} 0 & \Omega_P^* & 0 & 0 \\ \Omega_P & -2\Delta_P & \Omega_{C,5/2}^* & 0 \\ 0 & \Omega_{C,5/2} & -2(\Delta_P + \Delta_C) & \Omega_{C,3/2}^* \\ 0 & 0 & \Omega_{C,3/2} & -2(\Delta_P + \Delta_C + \Delta_{hfs}) \end{pmatrix}. \quad (5)$$

Where  $\Omega_P$ ,  $\Omega_{C,5/2}$  and  $\Omega_{C,3/2}$  are the Rabi frequencies associated with the 780 nm probe and 480 nm coupling  $45D_{5/2}$  and  $45D_{3/2}$  transitions respectively. In the calculations we assume that the probe (IR) laser is resonant  $\Delta_P = 0$ , the coupling (blue) laser frequency is varied in the range  $\Delta_C = \pm 300$  MHz. All atomic parameters, such as the dipole moments of atomic transitions and the hyperfine splitting of the  $45D_{3/2}$  and  $45D_{5/2}$  Rydberg state  $\Delta_{hfs} = 128$  MHz are calculated using Alkali-Rydberg Calculator (ARC) [20]. To determine the effective values of the probe and coupling fields Rabi frequencies, we optimize the values of  $\Omega_P$  and  $\Omega_{C,5/2}$  such that the ratio of amplitudes for  $45D_{5/2}$  peak and  $45D_{3/2}$  peak, as well as the width of  $45D_{5/2}$  peak match the experimental spectra for the counter-propagating geometry. Since the same physical coupling field couples both Rydberg state fine structure levels, the value of  $\Omega_{C,3/2}$  is proportional to  $\Omega_{C,5/2}$ . The same values of Rabi frequency are then used for all remaining simulated spectra. To account for the angle between the two optical fields in the model, we fix the direction of the probe field wave vector, and decompose the coupling field wave vector into a parallel and perpendicular components, and use the built-in Doppler averaging tools within Rydiqule to calculate EIT spectra [21]. When calculating the atomic absorption in the non-collinear geometry, we accounted for the reduced interaction volume of the two laser beams, and scaled the atomic density in the model accordingly. For simplicity we approximated the beams by perfect cylinders with the diameters equal to the full width half maximum of the laser beams, and calculated the overlapping volume of the two cylinders crossed at angle  $\phi$  using the built-in *RegionIntersection* function in Mathematica.

The results of the numerical modeling are shown in Fig.2 and show good agreement with the experimental data. When showing the resonance amplitudes, we set the height of the EIT peak in the counter-propagation geometry ( $\phi = 0$ ) to 100% (the best case scenario), and scale all the other resonance amplitudes relative to its value. As expected, the amplitude drops rapidly as soon as even a small angle is introduced. Similar reduction happens if the laser beams are originally co-propagating: the EIT peak has a local maximum for  $\phi = 180^\circ$ , that is approximately 30 % of the counter-propagating beam, and falls quickly as the angle between the beams increases. Similarly, the EIT resonances are the narrowest in either counter-propagating ( $\gamma_{EIT}(\phi = 0) \approx 10$  MHz) or co-propagating ( $\gamma_{EIT}(\phi = 180^\circ) \approx 30$  MHz) geometries, and grows almost linearly with the angle. Larger uncertainties in the resonance width at larger deviations are due to low EIT peak contrast in these points. One can see that the numerical results match the experimental results quite well, particularly for the resonance width. Some deviations in the resonance amplitude is expected, as in the model we did not take into account the Gaussian intensity profiles of the laser beams and their effect on the effective overlap volume calculations.

One of the advantages of using the crossed laser beams is the ability to carry out more localized measurements, as the

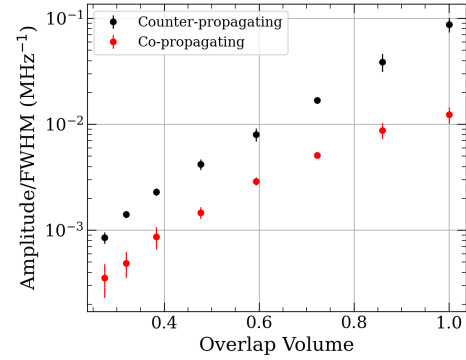


**Fig. 4.** Trade-off between the spectroscopic and spatial resolution of the crossed-beam EIT resonances. Here we use the experimentally measured ratios between the resonance relative amplitude and width, shown in Fig. 2 as a figure of merit for spectroscopic resolution. To characterize the spatial resolution, we use the calculated values of the overlap volume of the two laser beams relative to that in the collinear geometry  $\pi d^2 L_{cell} / 4 \approx 7 \text{ mm}^3$ .

overall EIT resonance is affected only by the electric fields in the volume where both probe and coupling fields are present. Clearly, there is a trade-off between the spatial and spectral resolution: larger angle between the two beams decreases the sensing volume, but at the same time makes the resonances broader and weaker. To characterize both performances we need to choose relevant figures of merit. The ratio between the EIT peak width and amplitude, sometimes referred as a resonance quality factor, is often used to characterize the spectral sensitivity, as in the case of a Lorentzian peak it is proportional to the slope of the discrimination curve for a standard phase-sensitive detection. For the spatial resolution it is logical to use the intersecting volume of the two beams. The relations between these two factors for both geometries are shown in Fig.4. As expected, the spectral resolution falls quite rapidly compare to the reduction of the sensing volume. However, thanks to the Gaussian intensity distribution of the laser beams and non-linear nature of EIT resonance, the actual spatial resolution may be better, and its more accurate characterization will be a subject of further studies.

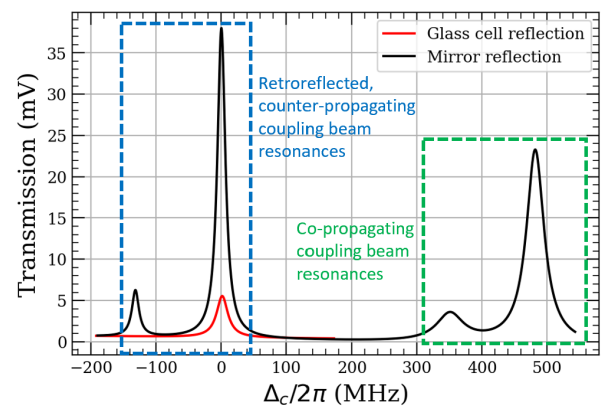


**Fig. 5.** Traces of EIT resonances recorded in co-propagating geometry with a coupling laser beam reflected back by exit glass window of the Rb vapor cell and by a dichroic mirror after the cell.

During the experiment we found an interesting possibility to simultaneously observe EIT resonances in both co- and counter-propagating geometries by retroreflecting the coupling beam through the cell. This effect is more notable in the co-propagating geometry with the natural reflection from the output cell window, since even a relatively weak reflected counter-propagating blue laser beam creates a visible EIT resonance, shown in Fig. 5. This additional resonance becomes more pronounced if the blue laser is intentionally retroreflected with a dichroic mirror. To ensure spectral separation of the resonances in different geometries, it is necessary to introduce some non-zero detuning of the probe field from the optical resonance  $\Delta_P$ . In this case, the optical response comes primarily from the atoms with the longitudinal velocities  $v_{\parallel} \approx \Delta_P/k_P$ . For such atoms the coupling field detuning required to fulfill EIT conditions depends on the field's propagation direction:  $\Delta_C = \pm \frac{k_C}{k_P} \Delta_P = \pm \frac{\lambda_P}{\lambda_C} \Delta_P$ . Such ability of creating multiple Rydberg EIT resonances may be useful as a tool of probing interactions in different spectral channels [22].

In conclusion, we experimentally and theoretically analyzed how the two-photon Rydberg EIT resonance lineshape changes depending on the angle between the probe and coupling laser field. We observed rapid deterioration in both resonance linewidth and amplitude even for a small relative angle for both nearly counter-propagating and co-propagating arrangements, and we explained this observation by the introduction of the transverse velocity-selective shift of the EIT resonances. The results of the numerical model are in good agreement with the experimental observation. Our findings may be useful for development for optimization of the non-collinear Rydberg EIT applications for localized rf or electric field measurements, as they allow to estimate the necessary compromise between the need of larger crossing angle to improve the spatial resolution and the accompanying deterioration of spectral EIT characteristics. We close by noting that the trade-off between spatial and spectral resolution of the non-collinear geometry can be eliminated, in principle, by using a three-photon Rydberg EIT transition with a Doppler-suppressing three-laser "star" configuration [3, 23].

**Funding.** This work is supported by NSF award 2326736, U.S. DOE Contract No. DE-AC05-06OR23177 and William & Mary through the Summer Undergraduate Research program.

**Acknowledgment.** We thank Dr. Nikunj Prajapati for useful discussions, and Ziqi Niu for help with the experimental equipment.

**Disclosures.** The authors declare no conflicts of interest.

## REFERENCES

1. T. F. Gallagher, *Rydberg Atoms*, Cambridge Monographs on Atomic, Molecular and Chemical Physics (Cambridge University Press, 1994).
2. C. L. Holloway, M. T. Simons, J. A. Gordon, *et al.*, "Electric field metrology for SI traceability: Systematic measurement uncertainties in electromagnetically induced transparency in atomic vapor," *J. Appl. Phys.* **121**, 233106 (2017).
3. N. Thaicharoen, K. R. Moore, D. A. Anderson, *et al.*, "Electromagnetically induced transparency, absorption, and microwave-field sensing in a rb vapor cell with a three-color all-infrared laser system," *Phys. Rev. A* **100**, 063427 (2019).
4. C. T. Fancher, D. R. Scherer, M. C. S. John, and B. L. S. Marlow, "Rydberg atom electric field sensors for communications and sensing," *IEEE Trans. on Quantum Eng.* **2**, 1–13 (2021).
5. A. P. Rotunno, C. L. Holloway, N. Prajapati, *et al.*, "Investigating electromagnetically induced transparency spectral lineshape distortion due to non-uniform fields in Rydberg-atom electrometry," *J. Appl. Phys.* **134**, 084401 (2023).
6. C. L. Holloway, J. A. Gordon, A. Schwarzkopf, *et al.*, "Sub-wavelength imaging and field mapping via electromagnetically induced transparency and autler-townes splitting in rydberg atoms," *Appl. Phys. Lett.* **104**, 244102 (2014).
7. L. A. Downes, A. R. MacKellar, D. J. Whiting, *et al.*, "Full-field terahertz imaging at kilohertz frame rates using atomic vapor," *Phys. Rev. X* **10**, 011027 (2020).
8. L. A. Downes, L. Torralbo-Campo, and K. J. Weatherill, "A practical guide to terahertz imaging using thermal atomic vapour," *New J. Phys.* **25**, 035002 (2023).
9. M. O. Scully and M. S. Zubairy, *Quantum Optics* (Cambridge University Press, 2001).
10. R. Finkelstein, S. Bali, O. Firstenberg, and I. Novikova, "A practical guide to electromagnetically induced transparency in atomic vapor," *New J. Phys.* **25**, 035001 (2023).
11. J. Keaveney, A. Sargsyan, D. Sarkisyan, *et al.*, "Active narrowband filtering, line narrowing and gain using ladder electromagnetically induced transparency in an optically thick atomic vapour," *J. Phys. B: At. Mol. Opt. Phys.* **47**, 075002 (2014).
12. N. DeStefano, S. Pegahan, A. Ramaswamy, *et al.*, "Electron beam characterization via quantum coherent optical magnetometry," *Appl. Phys. Lett.* (under review, 2024).
13. S. Mordjick, I. Novikova, E. Mikhailov, and S. Aubin, "Optical quantum sensing diagnostic development for non-invasive measurements of electric and magnetic fields in plasmas," DOE BRN Workshop on Measurement Innovation, Washington, D.C., Jan. 9, 2024.
14. N. Thaicharoen, K. R. Moore, D. A. Anderson, *et al.*, "Electromagnetically induced transparency, absorption, and microwave-field sensing in a rb vapor cell with a three-color all-infrared laser system," *Phys. Rev. A* **100**, 063427 (2019).
15. N. Prajapati, N. Bhusal, A. P. Rotunno, *et al.*, "Sensitivity comparison of two-photon vs three-photon Rydberg electrometry," *J. Appl. Phys.* **134**, 023101 (2023).
16. P. B. Weichman, "Doppler sensitivity and resonant tuning of rydberg atom-based antennas," *J. Phys. B: At. Mol. Opt. Phys.* **57**, 165501 (2024).
17. H.-J. Su, J.-Y. Liou, I.-C. Lin, and Y.-H. Chen, "Optimizing the rydberg eit spectrum in a thermal vapor," *Opt. Express* **30**, 1499–1510 (2022).
18. A. P. Rotunno, A. K. Robinson, N. Prajapati, *et al.*, "Inverse transform sampling for efficient Doppler-averaged spectroscopy simulations," *AIP Adv.* **13**, 075218 (2023).
19. O. Firstenberg, C. S. Adams, and S. Hofferberth, "Nonlinear quantum optics mediated by rydberg interactions," *J. Phys. B: At. Mol. Opt. Phys.* **49**, 152003 (2016).
20. N. Šibalić, J. Pritchard, C. Adams, and K. Weatherill, "Arc: An open-source library for calculating properties of alkali rydberg atoms," *Comput. Phys. Commun.* **220**, 319–331 (2017).
21. B. N. Miller, D. H. Meyer, T. Virtanen, *et al.*, "Rydiqule: A graph-based paradigm for modeling rydberg and atomic sensors," *Comput. Phys. Commun.* **294**, 108952 (2024).
22. S. Berweger, A. B. Artusio-Glimpse, N. Prajapati, *et al.*, "Independent rydberg atom sensing using a dual-ladder scheme," *Appl. Phys. Lett.* **124**, 184001 (2024).
23. I. I. Ryabtsev, I. I. Beterov, D. B. Tretyakov, *et al.*, "Doppler- and recoil-free laser excitation of rydberg states via three-photon transitions," *Phys. Rev. A* **84**, 053409 (2011).